Supporting Information

Stable Superhydrophobic Ceramic-based Carbon Nanotube Composite Desalination Membranes

Yingchao Dong[*a], *Lining Ma*[a], *Chuyang Y. Tang*[b], *Fenglin Yang*[a], *Xie Quan*[a], *David Jassby*[c], *Michael J. Zaworotko*[d] *and Michael D. Guiver*[**e]

[a] Key Laboratory of Industrial Ecology and Environmental Engineering (Ministry of Education, MOE), School of Environmental Science and Technology, Dalian University of Technology, Dalian 116024, China

[b] Department of Civil Engineering, The University of Hong Kong, Pokfulam, Hong Kong, China

[c] Department of Civil and Environmental Engineering, University of California Los Angeles, Los Angeles 159310, United States of America State

[d] Department of Chemical & Environmental Sciences, Bernal Institute, University of Limerick, Limerick V94 T9PX, Republic of Ireland

[e] Key Laboratory of Engines, and Collaborative Innovation Center of Chemical Science and Engineering (Tianjin), Tianjin University, Tianjin 300072, China

Corresponding authors:

Prof. Yingchao Dong

Key Laboratory of Industrial Ecology and Environmental Engineering (Ministry of Education, MOE), School of Environmental Science and Technology, Dalian University of Technology, Dalian 116024, China

Tel: +86-411-84706328 E-mail: ycdong@dlut.edu.cn

Prof. Michael D. Guiver

State Key Laboratory of Engines, and Collaborative Innovation Center of Chemical Science and Engineering (Tianjin), Tianjin University, Tianjin 300072, China

Tel: +86-158-22869113 E-mail: michael.guiver@outlook.com; guiver@tju.edu.cn

S1 Fabrication and characterization of hollow fiber ceramic substrate

S1.1 Materials and chemicals

Abundantly available bauxite (Yangquan, Shanxi Province, China) and NiO (99%, analytical reagent, Sinopharm Chemical Reagent Co., Ltd., China) were used as the raw materials for the preparation of low-cost hollow fiber spinel-based ceramic substrates by the phase inversion and sintering techniques (Fig. S1). Polyethersulfone (PES, technical pure grade, Radel A-100, Solvay Advanced Polymers, L.L.C.), N-methyl-2-pyrrolidone (NMP, chemical pure grade, Sinopharm Chemical Reagent Co., Ltd., China) and polyvinylpyrrolidone (PVP, chemical pure grade, Sinopharm Chemical Reagent Co., Ltd, China) were used as the binder, solvent, and additive, respectively. Deionized water was produced in our laboratory by a double-stroke ion exchanger (YF 02-01, Green Water Treatment Technology Co. Ltd., China).

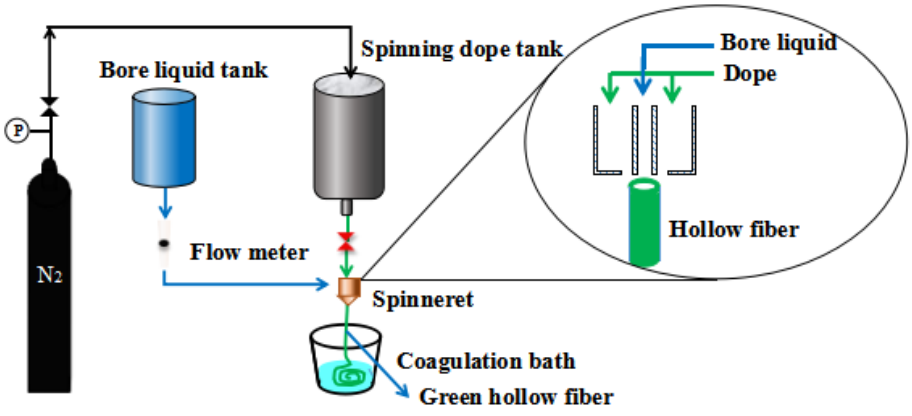

Figure S1. Schematic diagram of experimental set-up for fabrication of hollow fiber porous spinel-based ceramic substrates by a sequential process of dry-wet spinning and immersion-induced phase inversion.

The chemical composition of bauxite is shown in Table S1, determined by semi-quantitative X-ray fluorescence spectroscopy (XRF, Axios-Advanced, PAN

analytical, The Netherlands). Bauxite is composed mainly of Al_2O_3 (85.69 wt. %) and SiO_2 (7.33 wt. %). Theoretically, the mass percentages of alumina and mullite are calculated to be 67 wt. % and 26 wt. %, respectively. The crystal structure and the phase transformation were identified by X-ray diffraction (XRD, D/Max-2400 Rigaku Corporation, Tokyo, Japan). Fig. S2a displays the XRD pattern of bauxite, where the major crystalline phases are corundum (α-Al_2O_3, PDF#83-2080) and mullite ($3Al_2O_3 \cdot 2SiO_2$, PDF#83-1881). The mass percentages of corundum and mullite, based on the normalized reference intensity ratio (RIR) method[1] by processing the XRD result are determined to be 81 wt. % and 19 wt. %, respectively, which are to some extent different from the results derived from the XRF analysis due to variances between these two methods. The particle size distribution of bauxite was determined using a laser particle size analyzer (Mastersizer 2000, Malvern Instruments Ltd., UK). As shown in Fig. S2b, D_{50} of bauxite is around 2.0 μm. In spite of the presence of two main particle size distribution peaks, the bauxite exhibits a relatively narrow particle size distribution ranging from 1.0 to 4.0 μm.

Table S1. Chemical composition (wt. %) of the as-received calcined bauxite powder determined by semi-quantitative XRF.

Materials	Chemical composition										
	Al_2O_3	SiO_2	TiO_2	Fe_2O_3	K_2O	MgO	Na_2O	P_2O_5	CaO	SO_3	MnO
Bauxite	85.69	7.33	4.18	1.11	0.82	0.40	0.18	0.13	0.11	0.05	0.02

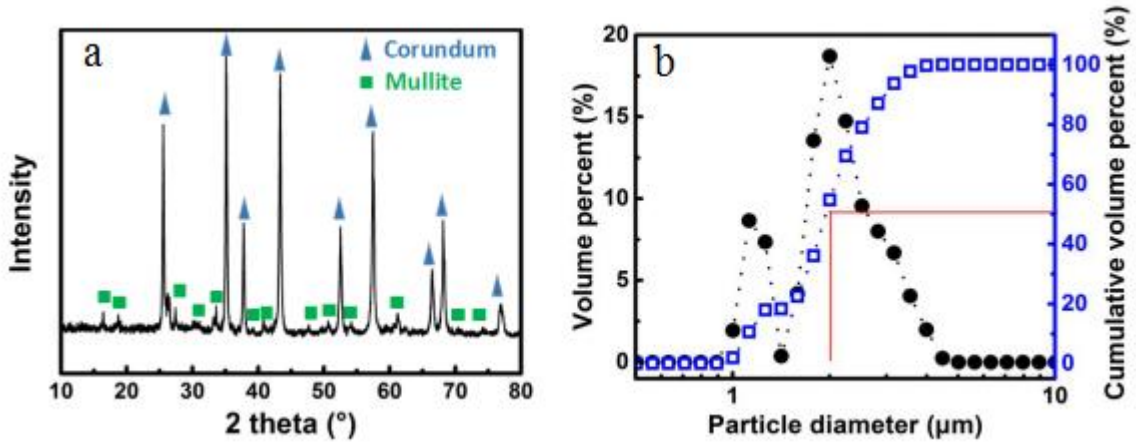

Figure S2. (a) XRD pattern, (b) particle size distribution of the as-received calcined bauxite powder.

Table S2. Dope compositions and dry-wet spinning conditions of hollow fiber porous spinel-based ceramic membrane substrates.

Parameter	Values
Dope compositions	
Bauxite + Nickel-oxide	60.0 wt.%
PES	8.0 wt.%
PVP	1.0 wt.%
NMP	32.0 wt.%
Spinneret dimension: ID/OD	1.3 mm / 2.5 mm
External/internal coagulant	Tap water / DI water
Spinning temperature	25 °C
Flow rate of internal coagulant	20 mL·min^{-1}
Air gap distance	15 cm
Nitrogen pressure	0.03 MPa

S1.2 Fabrication procedures of ceramic substrate

Nickel aluminate spinel hollow fiber membrane substrate was prepared by a dry-wet-spinning technique involving the immersion-induced phase inversion process (Fig. S1), based on optimized dope compositions and spinning conditions (Table S2). PES (8 wt.%) and PVP (1 wt.%) were dissolved in NMP (32 wt.%) under vigorous stirring. After a homogeneous polymer solution was formed, a mixture of bauxite and NiO (60 wt.%) powders was added according to an Al:Ni molar ratio of 4:1 based on the XRF result (Table S1). The spinning dope was wet-ball-milled at a rotation speed of 30 rpm for 48 h, followed by vacuum degassing at room temperature for 1 h. Immediately after degasification, the spinning dope suspension was extruded through a laboratory-made tube-in-orifice spinneret (the outer and inner diameters are 2.5 and 1.3 mm, respectively) with a nitrogen gas pressure of 0.3 bar. Deionized water and tap water were used as internal and external coagulant, respectively. After passing an air gap of 15 cm, the green-body hollow fibers were immersed into a tap water bath for 24 h to allow the completion of the phase inversion process, and then the fibers were dried in air at room temperature (25 °C). Finally, the prepared fiber membrane precursors were calcined in muffle furnace for 1.0 h at 200 °C and then 600 °C respectively, to remove residual water and the organic polymers (based on the TGA-DTA analysis in Fig. S3). The precursor fibers were then sintered at a certain temperature (in the range of 1200-1350 °C) for 2 h in air to obtain the final hollow fiber spinel-based ceramic substrates.

.

S1.3 DTA-TGA analysis of substrate green body

The DTA–TGA (Q50, TA Instrument Inc., USA) curves of the dried hollow fiber green body are presented in Fig. S3. The TGA curve indicates a minor mass loss of 1.8 wt.% between 30 and 200 °C, and a major mass loss of about 12.7 wt.% between 200 and 600 °C, which is ascribed to residual water and polymers, respectively. The major weight loss closely corresponds to the total weight percent of PES and PVP introduced in the suspension (13.4 wt.%, Table S2) and was accompanied by an exothermic peak at about 546 °C due to burning out of the PES and PVP polymers. Optimization of the temperature program, based on the DTA-TGA result, is necessary in order to control the polymer burnout process to avoid the formation of defects in the final ceramic substrates. For furnace calcination, a low heating rate of 2 °C·min^{-1} in the burnout region and a dwell time of 1.0 h at 200 °C and then 600 °C respectively were selected to minimize crack formation and collapse in the hollow fibers and to burn out organic polymers completely.

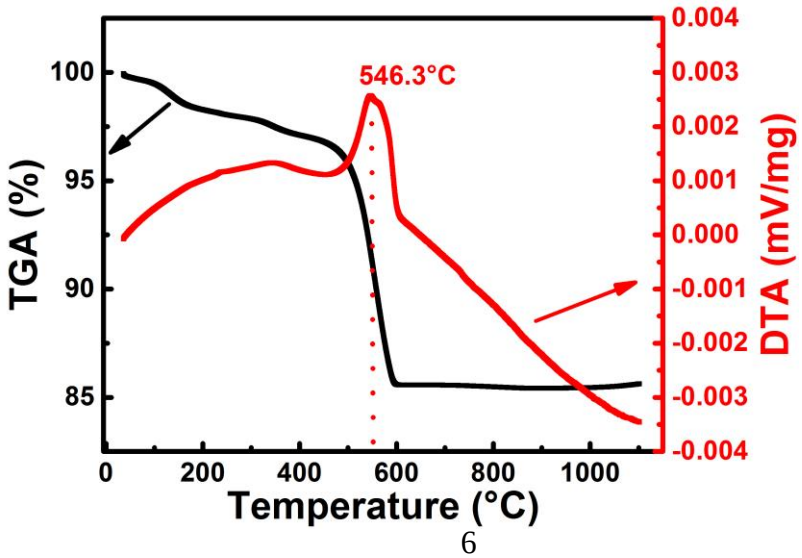

Figure S3. TGA-DTA curves of the dried hollow fiber spinel-based membrane substrate green body heated between 30 °C and 1100 °C in air with a constant heating rate of 10 °C·min^{-1}.

S1.4 Characterization and optimization of hollow fiber ceramic substrate

The effect of sintering temperature on XRD (XRD patterns and quantified phase content), pore size, SEM morphology, surface porosity and mechanical properties of the substrates were investigated in detail to obtain optimized structure and properties for subsequent fabrication of ceramic-CNT composite membranes.

S1.4.1 XRD analysis

Fig. S4 displays the XRD patterns and quantified phase contents of the spinel ceramic hollow fiber membranes after sintering at various temperatures (1100-1350 °C) for 2 h. At 1100 °C, $NiAl_2O_4$ (PDF#81-0718) was detected with a content of about 52%, which was formed through solid-state reactions between $3Al_2O_3{\cdot}2SiO_2$ and NiO (PDF#44-1159), and between Al_2O_3 and NiO.[2] With increasing temperature up to 1200 °C, the peak intensity of $NiAl_2O_4$ phase increases with a phase content of ~66%, and the NiO phase completely disappeared. When further increasing the sintering temperature above 1200 °C, the contents of $NiAl_2O_4$, Al_2O_3 and $3Al_2O_3{\cdot}2SiO_2$ phases were stable, at around 70%, 20% and 10%,

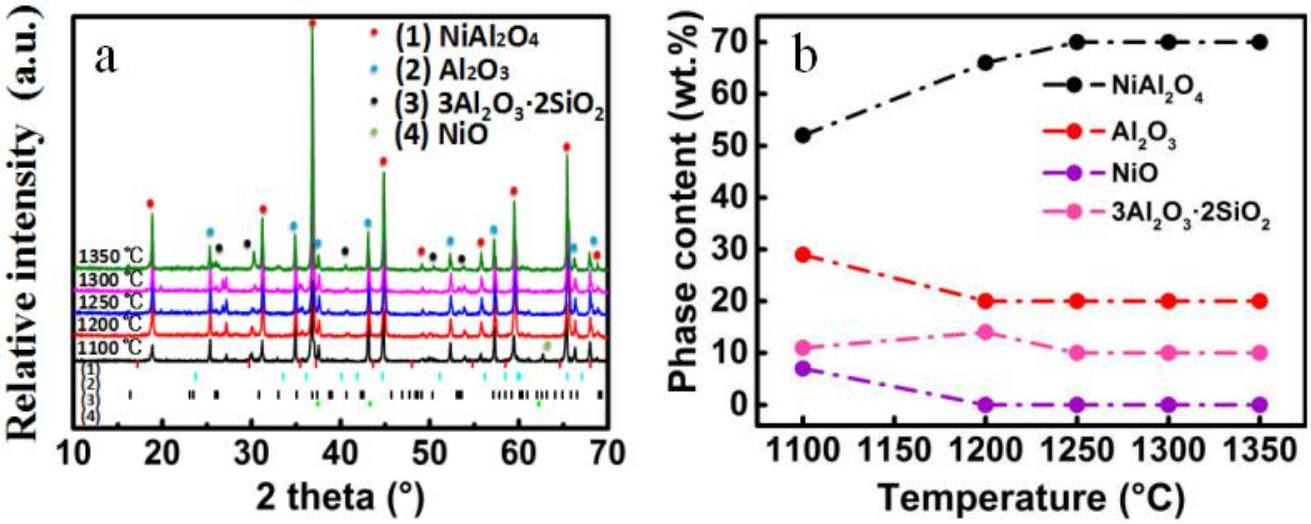

respectively.

Figure S4. (a) XRD patterns and (b) quantified phase contents (based on RIR method[1]) of the hollow fiber porous spinel-based ceramic membrane substrates after sintering in air at various temperatures ranging from 1100 to 1350 °C for 2 h.

S1.4.2 Pore size distribution

Pore size distribution is closely related to the sintering temperature. When the sintering temperature was 1200-1300 °C, the pore size distribution is narrow, as shown in Fig. S5a. The average pore sizes of the ceramic hollow fiber membranes (see Fig. S5b) were 506, 483 and 469 nm after sintering at 1200, 1250 and 1300 °C, respectively. A gradual decrease in average pore size with sintering temperature is observed due to sintering-induced volume shrinkage, leading to gradual densification. When the sintering temperature was increased to 1350 °C, the average pore size was dramatically decreased to 316 nm due to the growth of spinel particles, leading to the elimination of pores and formation of severe densification at high temperature.

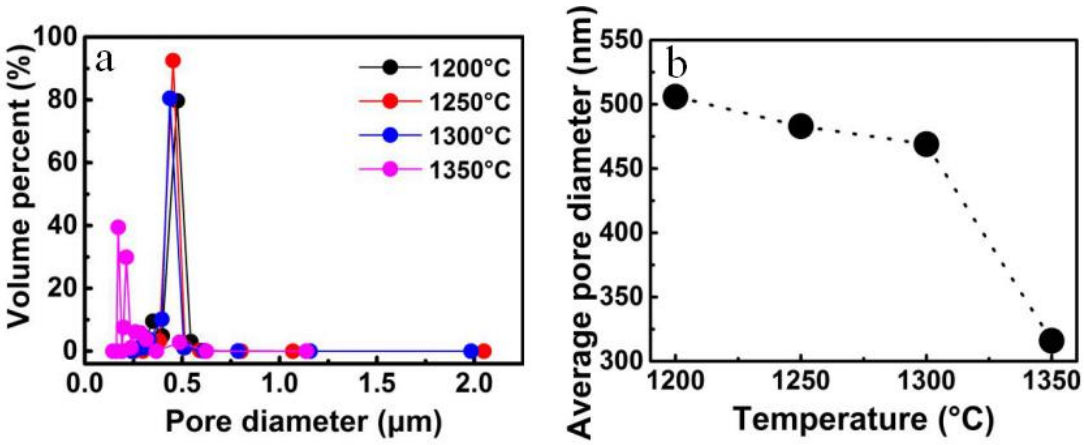

Figure S5. (a) Pore size distributions and (b) average pore size of the hollow fiber porous spinel-based ceramic membrane substrates after sintering in air at various temperatures

ranging from 1200 to 1350 °C for 2 h.

S1.4.3 SEM morphology and surface porosity

From Fig. S6a, it is observed that a porous structure is formed by partial-sintering of particle mixtures of bauxite and NiO at 1200 °C. From 1250 to 1300 °C (Figs. S6b and S6c), sintering gradually increases particle coalescence with slight densification, which is consistent with the pore size distribution results (Fig. S5a). With a further increase of sintering temperature up to 1350 °C, significant densification is observed, which results in a rapid decrease in both average pore size (Fig. S5b) and surface porosity, as discussed below (Fig. S7). The surface porosities of the inner and outer membrane surfaces and sponge-like regions at different sintering temperatures were quantified using the tool ImageJ[3], as shown in Fig. S7. The surface porosity of the membranes decreased with increasing temperatures. Compared with the porosity of the outer surface, the porosity of the inner surface is higher, and the porosity of the fractured surface of the sponge-like region is lower. During the fiber spinning process using a relatively large inner fluid velocity (20 $mL \cdot min^{-1}$), shear stresses act upon the inner surface, resulting in movement of unfixed particles to avoid the formation of a dense surface. Due to the large finger-like structures on both inner and outer surfaces, the porosity of the inner and outer surfaces is larger than the porosity of the fractured surface of the sponge-like regions.

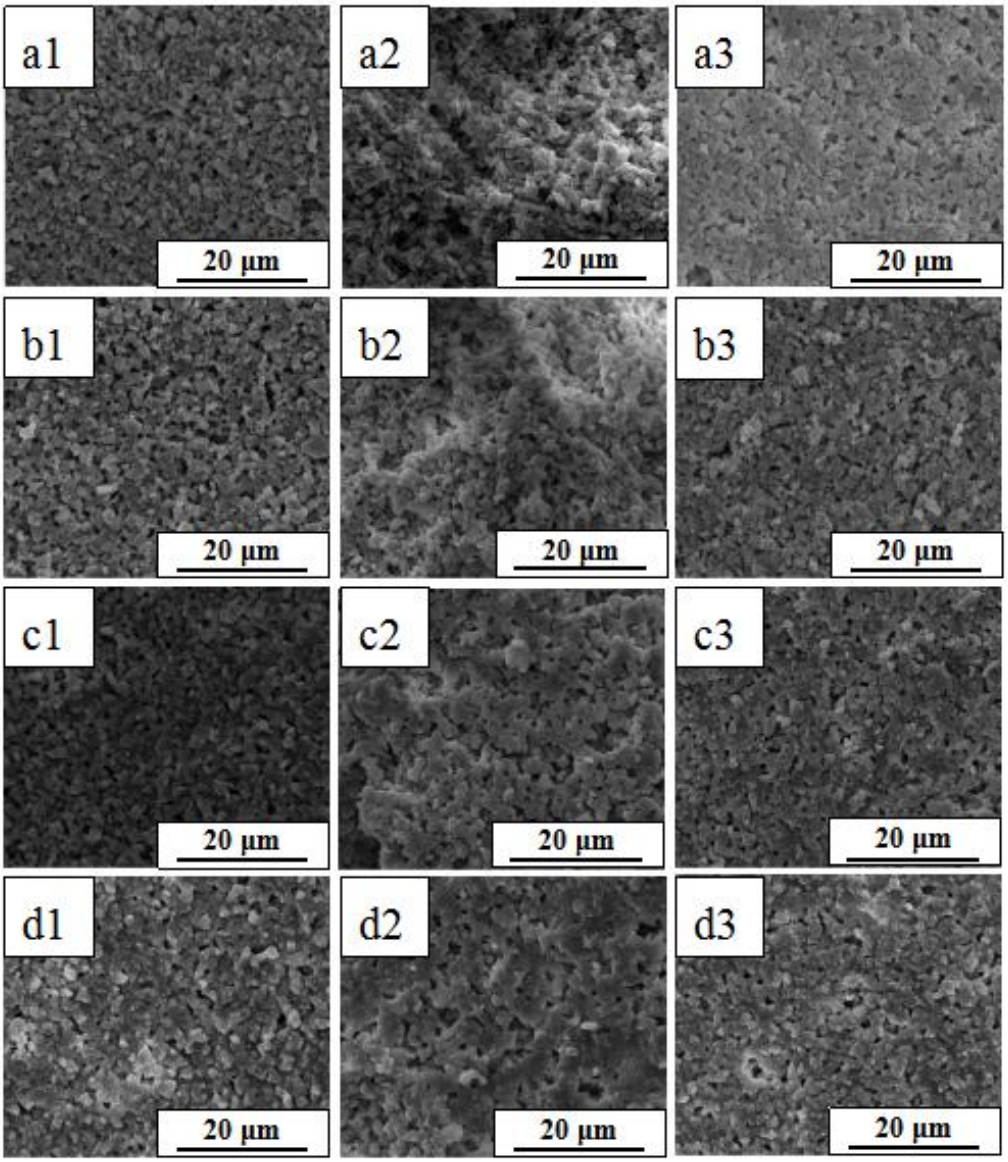

Figure S6. SEM images of the hollow fiber porous spinel-based ceramic membrane substrates after sintering in air at various temperatures (a) 1200 °C, (b) 1250 °C, (c) 1300 °C and (d) 1350 °C (1 inner surfaces, 2 fractured surface of the sponge-like regions, 3 outer surfaces).

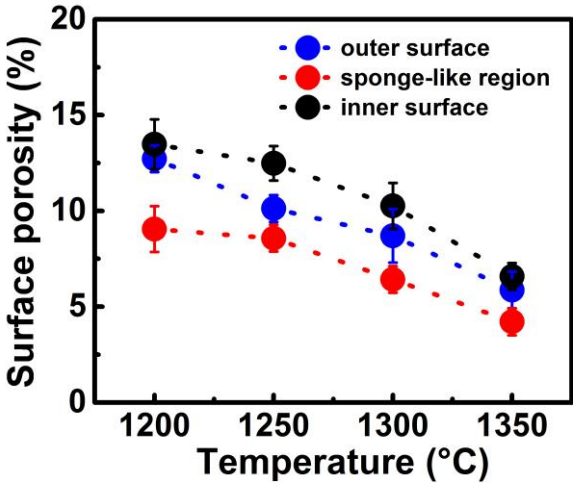

Figure S7. Quantified surface porosities processed from SEM images (in Fig. S6) by the tool ImageJ of the hollow fiber porous spinel-based ceramic membrane substrates after sintering in air at various temperatures ranging from 1200 to 1350 °C for 2 h.

S1.4.4 Mechanical properties

Sufficient mechanical and morphological stability are of paramount importance to ensure membrane durability and function. In particular, controlling the morphological stability of the *in situ* grown CNTs within the structures of the ceramic substrates is necessary for maintaining the integrity and function of the ceramic-CNT composite membranes (Fig. S17). The mechanical strength of the hollow fiber substrates was measured by the three-point bending strength method using a universal testing machine (AGS-X, Shimadzu Ltd., Japan). The substrate was placed on a span of 8 mm and was loaded at a crosshead speed of 0.02 mm·min^{-1} until fracture occurred. The bending strength, (σ_f), was calculated based on the following *Eq.S1*[4]

$$\sigma_f = \frac{8FLD}{\pi(D^4 - d^4)} \quad (S1)$$

Where *F* is the measured force when a fracture occurs (N), *L* is the span (8 mm), *D* and *d* are the outer and inner diameters of the hollow fiber, respectively.

Weibull analysis was conducted on the results of three-point bending strength. The Weibull analysis curves were made using lnσ and lnln[1/(1-P_f)] plot as X-axis and Y-axis respectively, where σ is the three-point bending strength, P_f is the fracture probability. The latter P_f is defined by *Eq.S2*

$$P_f = i / (N+1) \quad (S2)$$

where i is the rank in three-point bending strength from smallest to largest and N denotes the total number of samples (here N = 10 in our study).

Fig. S8 shows the mechanical property results of the ceramic hollow fibers after sintering at various temperatures (1100-1350 °C). In Fig. S8a, for all the fibers, a nonlinear monotonic relationship between load and deflection can be clearly observed before the maximum loads, which are then followed by a rapid load degradation. This is typical for brittle ceramics with porous structures. Figs. S8b and S8c show that the both three point bending strength and fracture energy are gradually improved with increasing sintering temperature. The bending strength of the fiber sintered at 1100 °C is approximately 12.0±1.6 MPa, which is lower than that (22.6±1.6 MPa) of the membrane sintered at 1200 °C. The likely reason for these very low bending strengths at 1100 °C and 1200 °C is that the packed particles were still weakly sintered. With increasing the sintering temperature from 1250 to 1300 °C, the mechanical strength increased from 51.3±4.3 MPa to 71.2±7.8 MPa, which can be ascribed both to an increase in densification and spinel phase content (see Fig. S4b). Higher spinel content, along with 10 wt.% mullite, imparts a strengthening effect on the hollow

fiber substrate, resulting in enhanced mechanical strength.[4, 5] In Fig. S8d, most of the Weibull statistic points (lnσ versus lnln[1/(1−Pf)]) center close to the corresponding fit lines, which proves a good reliability of the bending strength results.

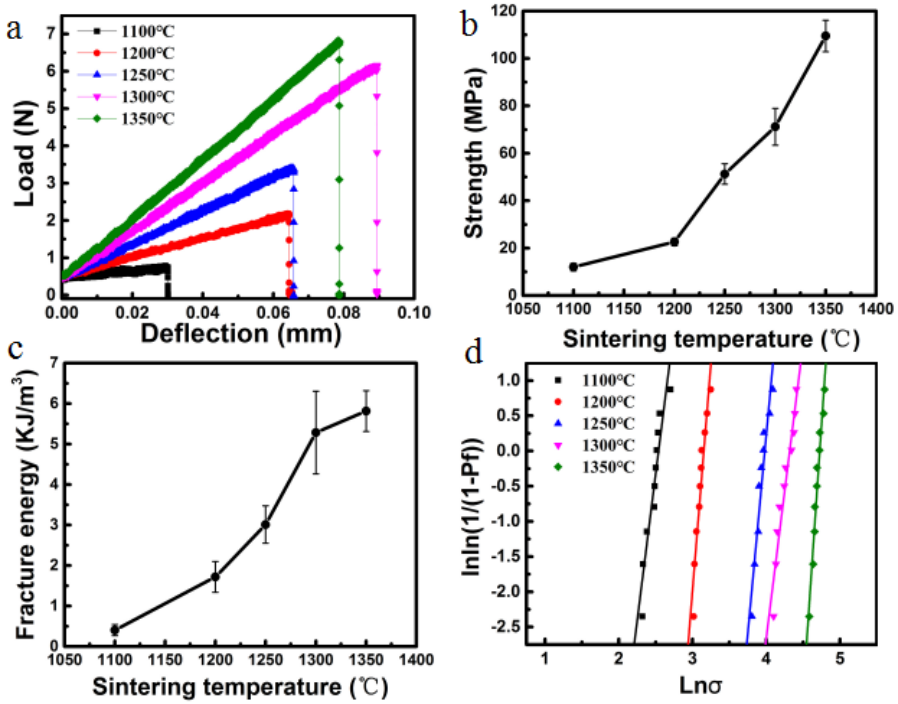

Figure S8. Mechanical strength tests of the hollow fiber spinel-based ceramic membrane substrates after sintering in air at various temperatures ranging from 1100 to 1350 °C for 2 h: (a) typical load-deflection curves, (b) three point bending strength versus sintering temperature, (c) fracture energy versus sintering temperature and (d) Weibull analysis of bending strength.

S1.4.5 Structure and properties of optimized ceramic substrate

The membrane substrate sintered at 1300 °C is considered as having the most appropriate optimized structure and properties for *in situ* construction of CNTs in the subsequent CVD process. Fig. S9a shows the substrate is well shaped in a regular hollow fiber configuration without any defects, where the outer/inner diameter and thickness are estimated to be 1.58/1.14 mm and 0.22 mm, respectively. Such a thickness as low as 0.22 mm (much lower than disc or tubular commercial membranes

(3-5 mm)), combined with long finger-like macro-voids, can significantly lower permeation resistance with shorter transport paths, showing high both water flux (7861 $L \cdot m^{-2} \cdot h^{-1}$) and N_2 gas flux (1166 $m^3 \cdot m^{-2} \cdot h^{-1}$) with an average pore size of 0.47 μm (Table S3). In addition, the effective membrane area per volume is as high as 4352 $m^2 \cdot m^{-3}$, which is higher than the range of other hollow fiber membranes (~2400-3600 $m^2 \cdot m^{-3}$) and significantly higher than commercial tubular (~400-650 $m^2 \cdot m^{-3}$) ceramic membranes (Table S4).[4, 6, 7]

A "finger-sponge-finger" asymmetric uniform morphology consisting of long finger-like macro-voids and thin sponge-like region is observed (Fig. S9b), which is a structure typical of hollow fibers prepared by the wet-drying-spinning method. The large-sized finger-like macro-voids originate from both the inner and outer fiber surfaces, occupying as high as about 77% of the whole cross-section, which significantly lowers gas transport resistance for methane/hydrogen during the subsequent CVD process, and water vapor in the DCMD operation. The sponge-like structure occupying only about 23% of the whole cross-section is located between the inner and outer finger-like macro-voids, providing the majority of mechanical strength (Fig. S8).

Formation of the membrane substrate morphological structure is related with the spinning dope viscosity. As the suspension dope is extruded, the outer and inner regions of the hollow fiber precursor have increased viscosity due to solvent evaporation and moisture effects, resulting in a slow diffusion of non-solvent. The finger-like macro-voids are thus formed due to a rapid exchange between solvent (NMP) and non-solvent (water), while sponge-like structures are formed due to a slow solvent – non-solvent exchange. The inner and outer surfaces, and fractured surface of

the sponge-like region present uniform porous microstructures with sintering necks as shown in the high magnification SEM images in Fig. S9c. The resulting high bending mechanical strength of 71.2±7.8 MPa achieved allows the substrate to withstand the tensile stress caused by *in situ* growth of CNTs within the substrate (Fig. S17). The corresponding surface porosities calculated via the ImageJ software are estimated to be 10.3 ± 1.2%, 8.7 ± 1.4% and 6.4 ± 0.7% for inner, outer, and fractured surfaces of the sponge-like region, respectively (Table S3).

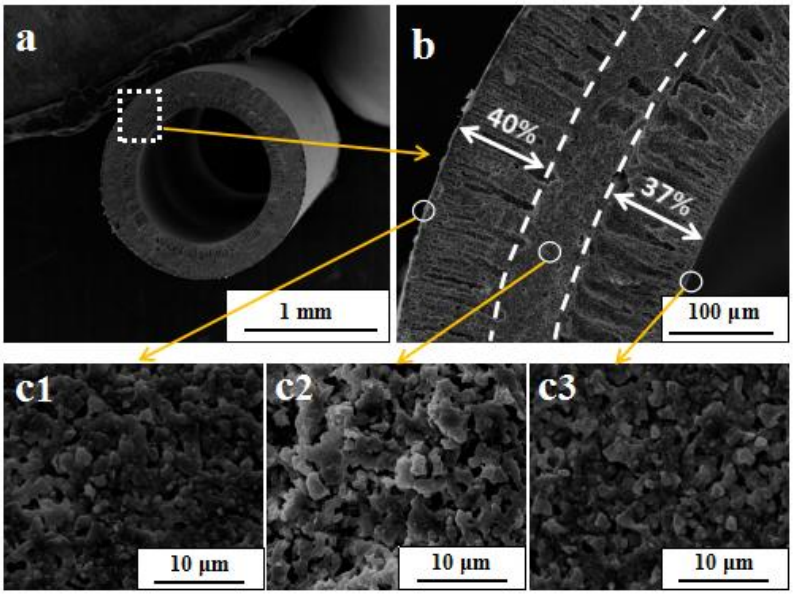

Figure S9. (a) Cross-sectional SEM image, (b) locally enlarged cross-sectional SEM image and SEM images of (c1) outer surface, (c2) fractured surface at sponge-like region and (c3) inner surface of the hollow fiber spinel-based ceramic membrane substrates at an optimized sintering temperature of 1300 °C for 2 h in air.

In summary, the prepared hollow fiber ceramic membrane substrates with a small wall thickness and high membrane area per unit volume (high packing density) have an asymmetric structure consisting of large-sized finger-like macro-voids, allowing low gas transport resistance for both the CVD reaction and DCMD operation, as well

as providing ample space for *in situ* growth of CNTs network to form a secondary superhydrophobic layer. Furthermore, ceramic membranes have some inherently robust properties: excellent durability with good mechanical integrity under harsh conditions such as high temperature, highly acidic, basic and salty environments, [8] which allows sufficient loading of catalyst precursor, *in situ* reduction of catalyst, subsequent high-temperature CVD reaction and final DCMD operation.

Table S3. Performances of the hollow fiber spinel-based ceramic membrane substrates (sintered in air at 1300 °C for 2 h)

Parameters	Values
Membrane area per volume /$m^2 \cdot m^{-3}$	4352
Surface porosity /%	10.3%, 8.7%, 6.4%
Pore size distribution /nm	244-612
Average pore size /nm	469
Pure water flux /$L \cdot m^{-2} \cdot h^{-1}$	7861
N_2 flux /$m^3 \cdot m^{-2} \cdot h^{-1}$	1166

Table S4. Comparison of packing density for different ceramic membranes (commercial tubular membranes, hollow fiber ceramic substrates in this work and in the reported literature).

Commercial tubular membranes*			Hollow fiber membranes			
7-C[#]	19-C	37-C	Al_2O_3[6]	YSZ[7]	Mullite[4]	Spinel this work

Packing density (m^2m^{-3})	429	561	634	2458	3599	3457	4352

*Great Wall Xinyuan Membrane Technology Co., Ltd., Hefei, Anhui Province, China

[#] C refers to the number of channels for commercial tubular multi-channel alumina ceramic membranes.

S2 Fabrication and characterization of ceramic-CNT composite membranes

S2.1 Materials and chemicals

High purity methane (CH_4, purity ≥ 99.999%), hydrogen (H_2, purity ≥ 99.999%) and nitrogen (N_2, purity ≥ 99.999%) were purchased from Zhonghao Guangming Research & Design Institute of Chemical Industry, China. Nickel (II) nitrate hexahydrate crystals ($Ni(NO_3)_2 \cdot 6H_2O$, analytical pure grade) was obtained from Shanghai Aladdin Bio-chem Technology Co., Ltd., China.

S2.2 Fabrication procedures and characterization of ceramic-CNT composite membranes

In situ construction of CNTs into ceramic hollow fiber substrate was carried out via methane CVD catalyzed by nickel nanoparticles, which were uniformly distributed over the surface of the membrane substrate and the pore walls of the long finger-like macro-voids. Ceramic hollow fiber membrane substrates were prepared by the immersion-induced phase inversion and sintering technique (see Fig. S1 and Section S1). Once prepared, hollow fiber substrates were initially rinsed with deionized water and absolute ethanol respectively for 30 min and completely dried at 60 °C for 60 min. To enable CNT *in situ* growth from the ceramic substrate, a nickel nano-catalyst was deposited on the ceramic surface. Nickel nitrate solution (5-40 wt. %) was introduced into the substrate using a simple vacuum impregnation method for 2 h, to ensure

sufficient loading of the catalyst precursor throughout the substrate. The substrate loaded with catalyst precursor was dried and calcined at 500 °C for 2 h in a quartz tube furnace, resulting in the formation of uniformly distributed NiO nanoparticles, followed by *in situ* reduction at 500 °C for 1 h in H_2 at a flow rate of 20 mL·min^{-1} to form Ni nano-catalyst (Fig. S12). CNTs were grown from the Ni nano-catalyst surface by chemical vapor deposition (CVD). A mixture of methane and hydrogen gases with a flow rate of 20 mL·min^{-1} was introduced into the tube furnace and the reaction was maintained at 450-850 °C for different dwell times ranging from 30 to 210 min, leading to *in situ* growth of CNT. After CVD reaction, nitrogen purge gas was used to cool the reactor to room temperature. Membranes with fully-covered and partially-covered CNT network structures are denoted as FC-CNT and PC-CNT, respectively. A schematic diagram of the CVD apparatus is shown in Fig. S10. Photographs of the hollow fiber dried green body, sintered spinel-based ceramic substrate, and final FC-CNT membranes after CVD reaction are shown in Fig. S11.

The morphologies of the prepared hollow fiber ceramic substrate, Ni nano-catalyst and ceramic-CNT composite membranes were observed by scanning electron microscopy (SEM, QUANTA 450, FEI, USA). The water contact angle was determined using an optical contact angle & interface tension meter (KINO SL 200KB, SoLon·TECH, Shanghai, China). To study accelerated thermal and superhydrophobic stability, the composite membranes were immersed in boiling water for several periods of time, up to 24 h, and the resulting water contact angle was measured for

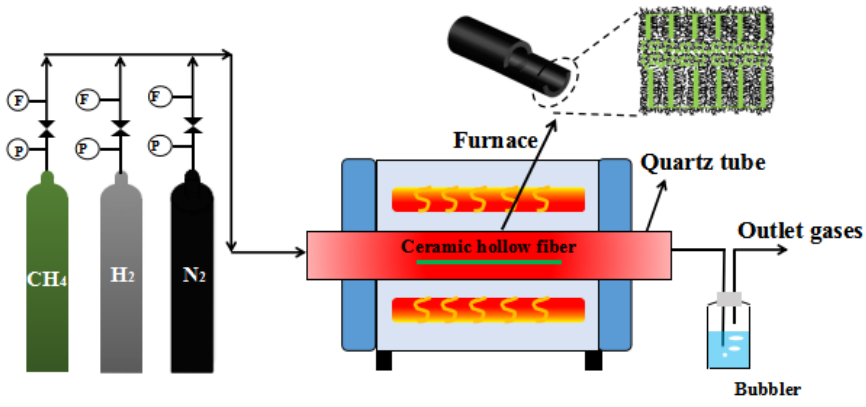

Figure S10. Schematic diagram of the CVD experimental apparatus for *in situ* growth of CNTs in hollow fiber spinel-based ceramic membrane substrates.

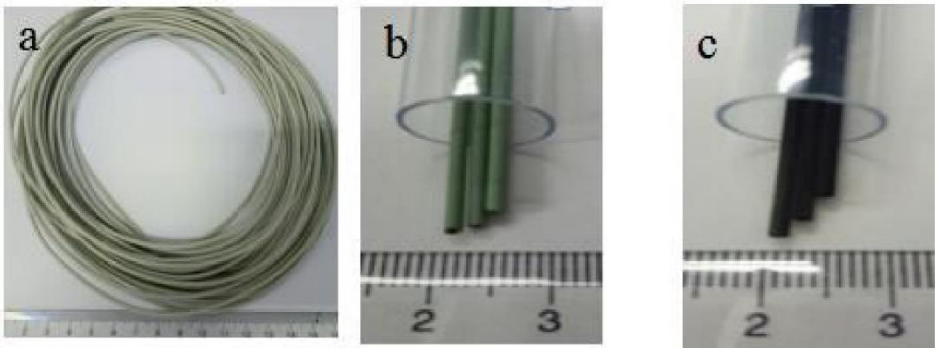

Figure S11. Photographs of the hollow fiber (a) dried green body before sintering, (b) sintered spinel-based ceramic membrane substrate, and (c) FC-CNT membranes after CVD reaction.

S2.3 SEM image and particle size of Ni nano-catalyst

CNT was grown *in situ* by thermal cracking of methane on Ni nano-catalyst, which was loaded on the surface of partially-sintered ceramic particles of hollow fiber membrane substrates. Until now, CNT has been grown on disc ceramic membranes having symmetric straight pore structures,[9, 10] which is different from the substrate used in this work. The present work applies vacuum impregnation to ensure sufficient penetration of catalyst precursor solution throughout the pores of the hollow fibers, finally resulting in the formation and deposition of Ni nano-catalysts with an average particle size of 24 nm, predominantly in the range of 10 to 30 nm (determined by Nano Measurer software) after drying and reduction at 500 °C in hydrogen gas (Fig.

S12). Abundant –OH groups inherent on the hydrophilic ceramic surface provide active sites for loading nano-catalyst precursors without the need for any surface modification, endowing good adhesion between substrate and Ni nano-catalyst, and therefore between substrate and *in situ* grown CNTs after CVD reaction.

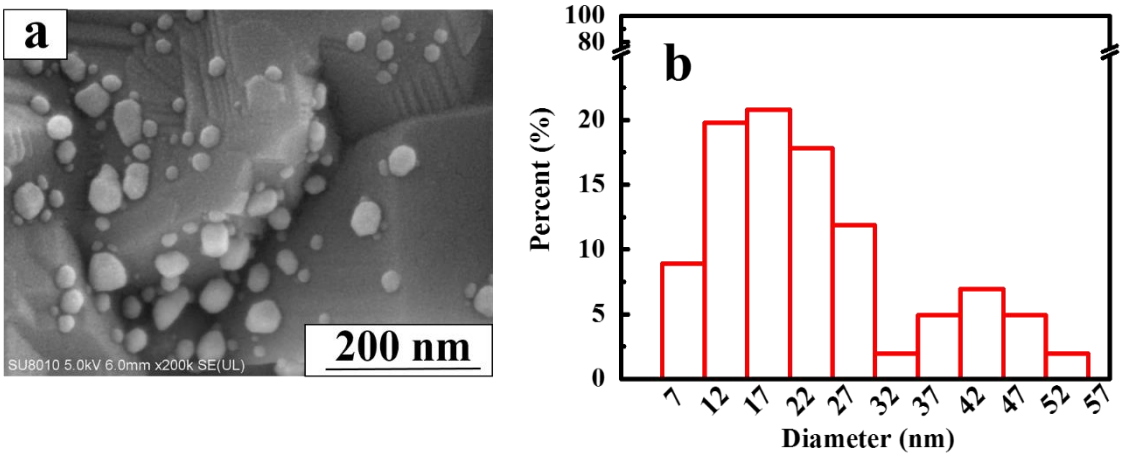

Figure S12. (a) SEM image and (b) particle size distribution of Ni nano-catalysts distributed inside the hollow fiber spinel-based ceramic membrane substrate.

S2.4 Characterization of CNTs in composite membranes

The XRD patterns of ceramic substrate, NiO-loaded substrate and ceramic-CNT (FC-CNT) composite membranes are shown in Fig. S13a. When comparing the ceramic substrates with and without NiO loading *via* vacuum impregnation of $Ni(NO_3)_2$ solution, it is observed that a new phase of NiO ($2\theta = 63.8°$) appears in the substrate after the impregnation-drying-calcination treatment, confirming that catalyst precursor was successfully vacuum-loaded within the ceramic substrate. The appearance of a reflection at $2\theta = 26.1°$ suggests the formation of CNTs after CVD reaction. Moreover, the reflections at $2\theta = 44.5°$ and 51.7° are attributed to metallic

nickel, indicating that NiO was completely reduced under the H_2 atmosphere. Raman spectroscopy (DXR Raman Microscope, Thermo Fisher Scientific Inc., USA) is a useful tool for characterization of CNT. As shown in Fig. S13b, three known bands at 1348 cm^{-1}, 1579 cm^{-1} and 2716 cm^{-1} (D, G and G' bands) are indicative of MWCNT (Multi-walled Carbon Nanotube) deposition within the substrate. The morphology of CNT was examined under transmission electron microscope (TEM, JEM-2010, JEOL Ltd., Japan). The *in situ* grown CNTs have a rope-like tubular structure with hollow core (Figs. S13c). Some of them even have compartment layers with a curvature directed towards the tip. The CNTs contain Ni nano-catalyst predominately at the root end with the tip end closed, indicating a base-growth mode.[11] This is probably due to the strong catalyst–substrate interaction in our work, which highly favors this growth model. In Fig. S13d, an HRTEM image of the prepared CNTs indicates very few defects and a high degree of crystallinity. This is also verified by the XRD results (see Fig. S13a). The *d*-spacing is estimated to be 0.33 nm, corresponding to the (002) reflection of ideal graphitic structure.

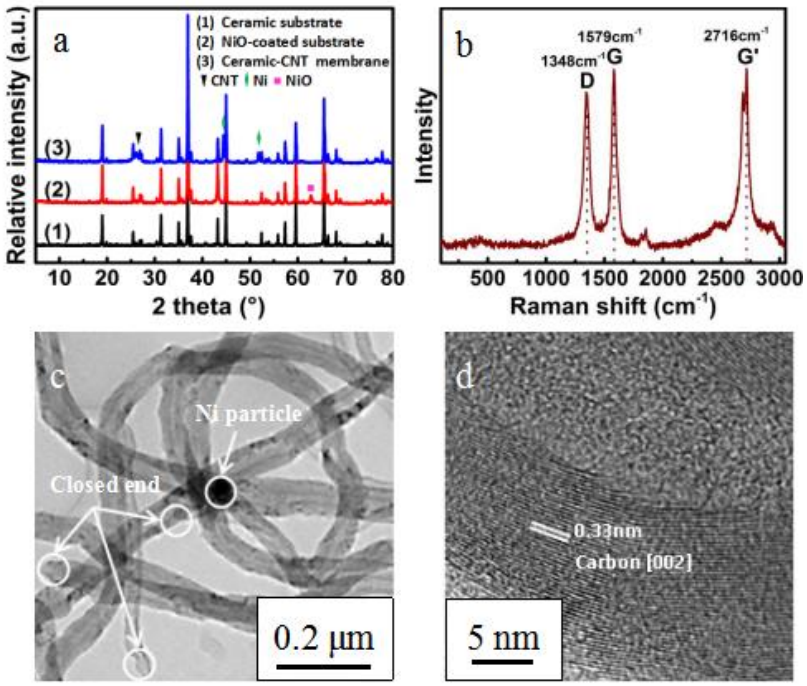

Figure S13. (a) XRD patterns of the hollow fiber spinel-based ceramic membrane substrate, NiO-loaded spinel-based ceramic membrane substrate and ceramic-CNT composite membranes, (b) Raman spectrum, showing the D, G and G' bands indicative of MWCNT (c) TEM and (d) HRTEM of CNTs of the ceramic-CNT composite membranes.

S2.5 Structure optimization of ceramic-CNT composite membranes

S2.5.1 Influence of Ni nano-catalyst loading

Fig. S14a displays the influence of Ni loading on CNT yield in the composite membrane eventually obtained at a CVD reaction temperature of 650 °C for 3 h. The yield of CNT increases with increasing Ni loading and reaches a plateau when the concentration is 30 wt.%. However, with a further increase of Ni loading, a decrease in the yield of CNT is observed, because the agglomeration of Ni nano-crystallites into larger particles is not conducive to CNT growth at higher nickel nitrate concentration. This turning point at 30 wt.% was subsequently taken as the upper-limit concentration for Ni loading. To identify membrane structures at different CNT yields, SEM images were taken from the surfaces of ceramic-CNT composite membranes (Figs. S14b, S14c and S14d). Low loading of Ni nano-catalyst results in the construction of a small quantity of fine and short CNTs with the presence of residual carbon, which partially covers the substrate. When Ni loading increases, both the length and covering density of CNT increase, due to an increase in the available active Ni nano-catalyst sites, thus allowing formation of a surface layer of randomly grown CNT network. Qualitatively, membrane structure can be identified as two distinct types: one is partially covered substrate CNT membrane (PC-CNT) at low Ni nano-catalyst loading (Figs. S14b and S14c), and the other is fully covered substrate

CNT membrane (FC-CNT) at high Ni nano-catalyst loading (Fig. S14d). The latter has an integrated defective layer of highly porous interconnected CNTs on the membrane surface. The obtained trends in this study are in good accordance with those of different substrate structures reported by Chen et al.[10]

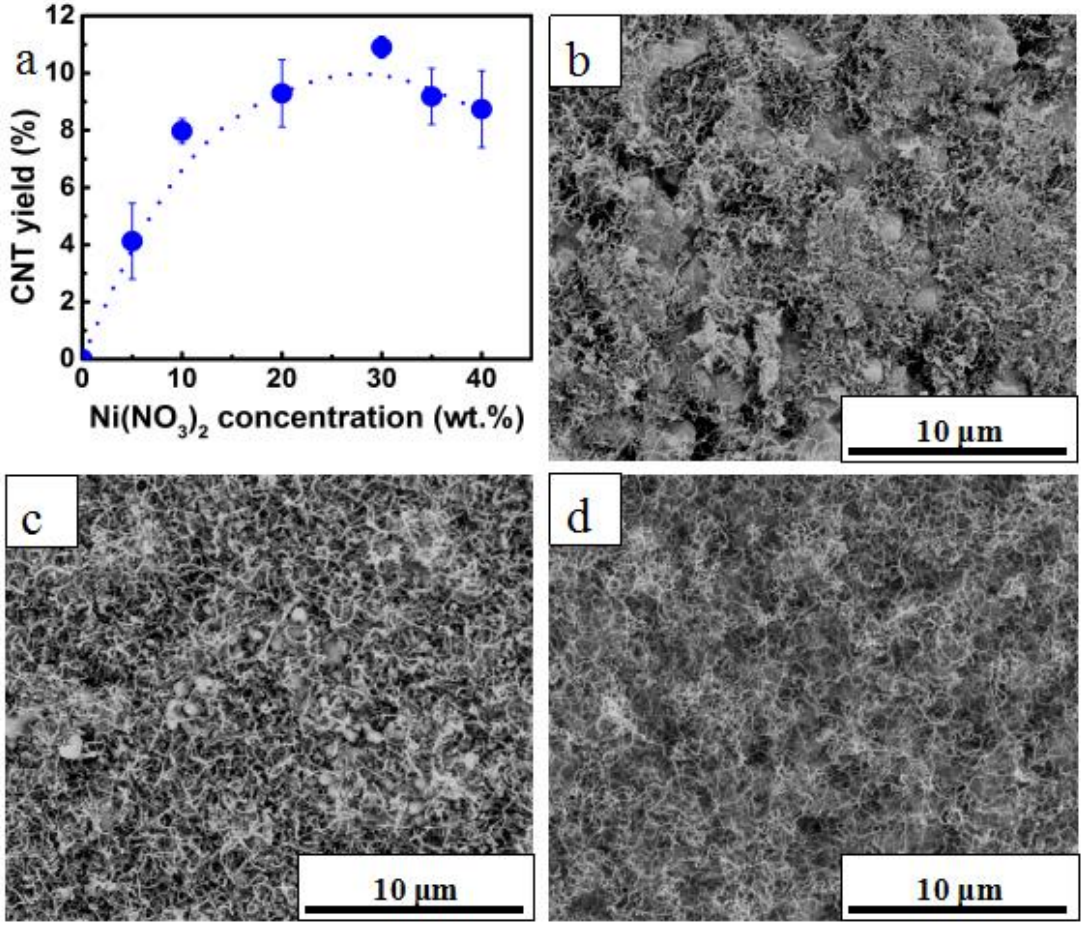

Figure S14. (a) CNT yield variation with $Ni(NO_3)_2$ concentrations for Ni nano-catalyst loading (CVD reaction temperature 650 °C, CVD reaction time 3 h), typical surface SEM images of the ceramic-CNT composite membranes fabricated using different $Ni(NO_3)_2$ concentrations: (b) 10 wt.%, (c) 20 wt.% and (d) 30 wt.%.

S2.5.2 Influence of CVD reaction temperature

Experiments were carried out at different CVD reaction temperatures for 3 h using the same Ni nano-catalyst loading (nickel nitrate concentration: 30 wt. %). The

results of CNT yield and SEM images of composite membranes as a function of temperature are shown in Fig. S15. Generally, increasing reaction temperature (below 700 °C) resulted in an increased CNT yield, especially at 550-700 °C. For example, a significant increase in CNT yield (10.8%) occurs from 550 °C to 700 °C, because catalytic decomposition of methane is an endothermic process, which is favored at higher temperatures.[12] An independent study has reported that Ni nanoparticles in a quasi-liquid state were readily broken into many finer particles at a high reaction temperature, resulting in a higher CNT growth rate and length.[13] At temperatures higher than 750 °C (Fig. S15a), however, besides a decreasing yield of CNT, an overgrowth of CNTs caused higher tensile stress within the membrane pores, consequently resulting in breakage of the composite membrane. Indeed, at temperatures higher than 750 °C, agglomeration into larger-sized particles results in partial deactivation of the Ni nano-catalyst.

Surface SEM images clearly show that reaction temperature significantly influences the yield and morphologies of CNT. It is observed that minimal CNT growth occurs at 550 °C (Fig. S15b), while CNT growth is evident at 650 °C (Fig. S15c), forming a continuous layer with a highly porous interconnected CNT network on the membrane surface, fully covering ceramic particles and open pores of the substrate. A temperature window of 600-750 °C is thus considered as the most suitable range for *in situ* construction of a continuous CNT network, without incurring membrane breakage. However, in order to produce a fully continuous CNT network layer along with good composite membrane integrity, 650 °C is considered as the optimum reaction temperature, which is also in accordance with the maximum activity for carbonization of methane at about 650 °C.[14]

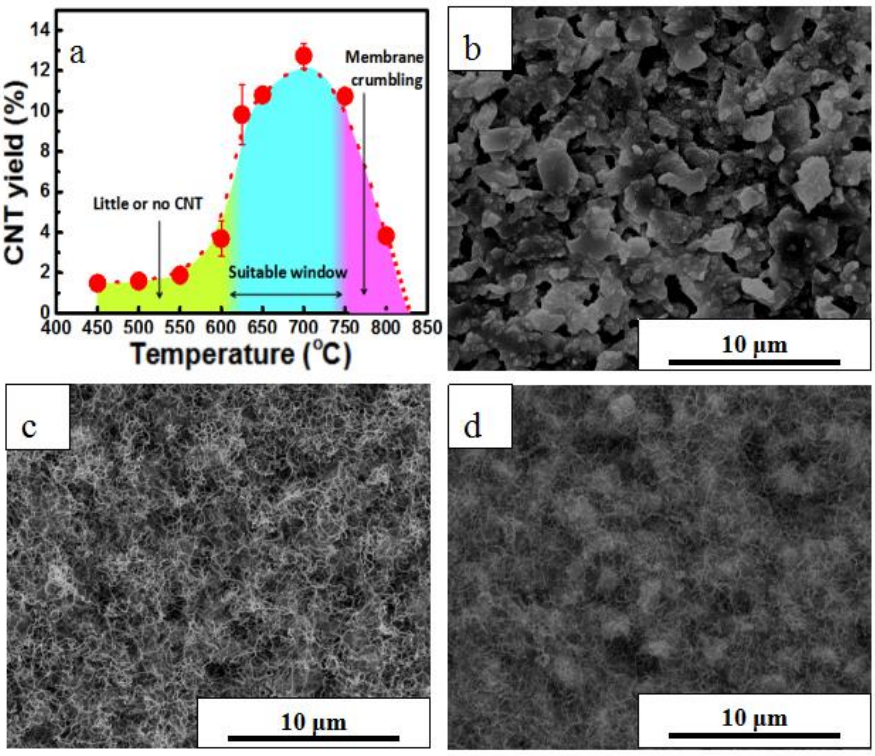

Figure S15. (a) CNT yield variation with CVD reaction temperature (nickel nitrate concentration 30 wt. % for Ni nano-catalyst loading, reaction time 3 h). Typical SEM surface images of the ceramic-CNT composite membranes fabricated at different CVD reaction temperatures for 3 h: (b) 550 °C, (c) 650 °C and (d) 750 °C.

S2.5.3 Influence of CVD reaction time

Fig. S16 displays the progression of CNT yield (wt.%) and surface SEM images with reaction time for the ceramic-CNT composite membranes fabricated at 650 °C. The CNT yield increases gradually from 4.8 wt.% to 10.1 wt.% with increasing

reaction time from 60 to 180 min (Fig. S16a). The SEM images taken from the surface of the ceramic-CNT hollow fiber reveal randomly interconnected CNT growth (Fig. S16). A shorter reaction time (45 min, Fig. S16b) resulted in the formation of PC-CNT membrane, while a prolonged reaction time resulted in formation of FC-CNT membrane (120 and 180 min, Figs. S16c and S16d). Abundant interconnected CNT entangled network layers are observed for growth times of 120 min and 180 min (Fig. S16d inset). This highly porous structure on the membrane surface, as well as in the pore walls of long finger-like macro-voids (Fig. S22) is necessary for effectively enhancing water vapor transport (due to high water-vapor interface), anti-wetting resistance (due to excellent thermal and superhydrophobic stability), and ensuring high performances in flux and rejection, as well as long-term stability for ceramic-CNT composite membranes in DCMD application. Although the CNT length increases with increasing reaction time above 195 min, it causes membrane crumbling (just like membrane breakage at higher reaction temperature, Fig. S15a) due to the restricted substrate pore space and increased tensile stress caused by CNT growth.

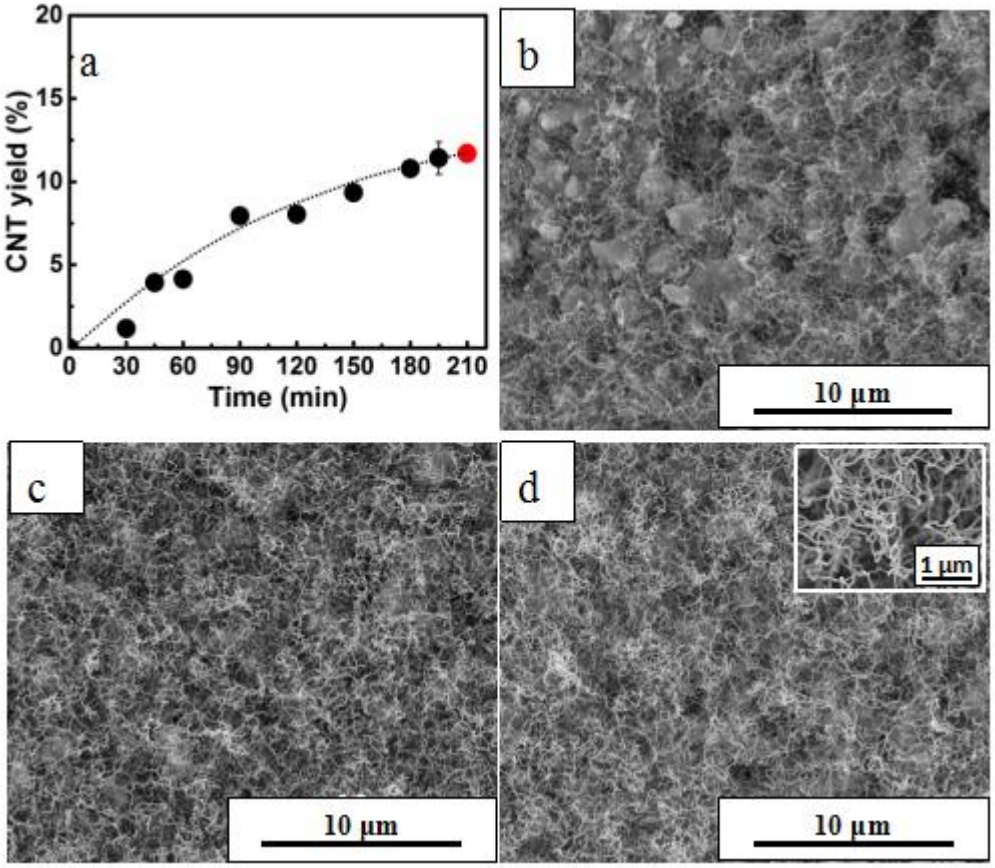

Figure S16. (a) Progression of CNT yield at different CVD reaction times (nickel nitrate concentration 30 wt.% for Ni nano-catalyst loading, CVD reaction temperature 650 °C), and typical surface SEM images of the ceramic-CNT composite membranes fabricated at 650 °C for different CVD reaction times (b) 45 min, (c) 120 min and (d) 180 min. The red solid circle in Fig. S16a indicates membrane crumbling at a long CVD reaction time of 210 min. The insert in Fig. S16d shows an enlarged surface SEM image of the ceramic-CNT membrane fabricated at a CVD reaction time of 180 min, having superporous membrane surface structure with randomly grown CNT networks.

S2.6. Breakage control of ceramic-CNT composite membranes

In our experiments on the fabrication of ceramic-CNT membrane via *in situ* growth of CNTs on/in the ceramic substrates, porous substrate breakage sometimes occurred during CVD, because of tensile stresses generated by overgrowth of CNTs in confined pore structures. The careful selection of the substrates with sufficiently good

mechanical properties (sintered at higher temperatures such as 1300 °C, Fig. S17b) combined with the careful control of CVD parameters such as reaction temperature (lower than 750 °C, Fig. S15a) and reaction time (less than 195 min, Fig. S16a) are of paramount importance in achieving structural integrity and function for the ceramic-CNT composite membranes. For instance, for the substrate sintered at 1250 °C, membrane breakage occurred at 51.3±4.3 MPa (measured by three-point bending strength), which is insufficient to withstand the tensile stresses generated during CNT growth (Fig. S17a). Integrated ceramic-CNT composite membranes were obtained when using substrates having higher mechanical strength (71.2±7.8 MPa) (Fig. S17b), prepared by sintering at 1300 °C.

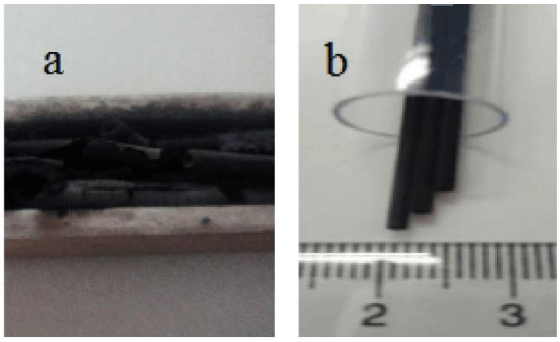

Figure S17. Photographs of the ceramic-CNT composite membranes fabricated with two different hollow fiber spinel-based ceramic membrane substrates sintered at (a) 1250 °C and (b) 1300 °C in air for 2 h.

S2.7 Pretreatment of ceramic-CNT composite membranes

To avoid any possible release of impurities such as residual carbon into water during DCMD operation, cleaning pretreatment of the ceramic-CNT membrane was performed by cross-flowing tap water at different flow rates (0 to 6.28 $m \cdot s^{-1}$) for 60 - 360 min. As presented in Fig. S18, a slight mass loss (0.65 - 0.97 wt.%) occurs in the first 60 min under different flow rates, which is attributed to the release of impurities

from the membrane. With further cleaning time, there is no further mass loss, even when exposed to a high flow rate of 6.28 $m \cdot s^{-1}$. This suggests there is good adhesion between the ceramic substrate and CNTs, endowing the ceramic-CNT membrane with excellent structural stability. It is worth mentioning that membrane distillation is not a filtration process, and detachment of membrane components is also strongly limited in absence of hydrostatic pressure. Hence, before the DCMD experiments were conducted, all the ceramic-CNT composite membranes were first pre-treated by tap water at a cross-flow rate of 6.28 $m \cdot s^{-1}$ for 120 min.

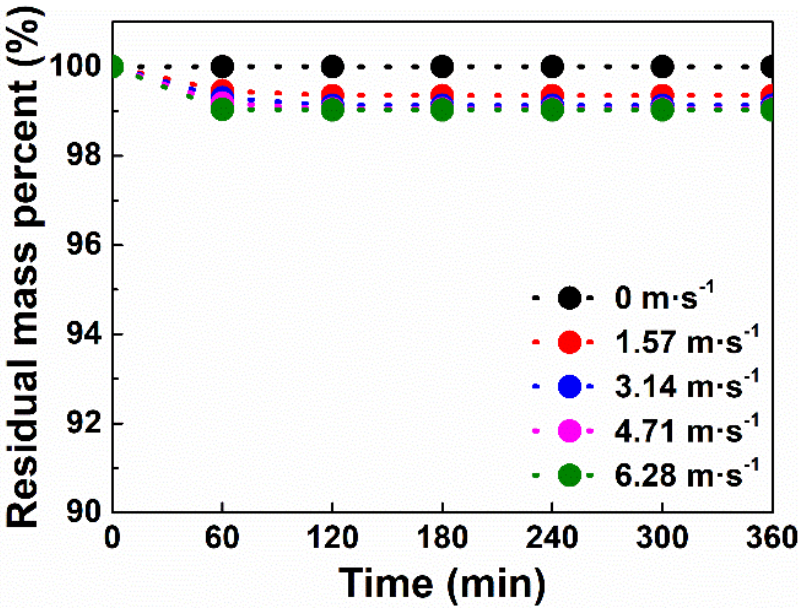

Figure S18. Effect of water flow time on residual mass percent of the ceramic-CNT composite membranes cleaned with tap water at different cross-flow rates in the range of 0 to 6.28 $m \cdot s^{-1}$.

S2.8 Water and N_2 permeability, pore size distribution of membranes

Schematic diagrams of the experimental apparati by dead-end model made in our laboratory, including water liquid entry pressure (LEP) and N_2 gas permeability tests, are shown in Fig. S19. The pore size distribution was measured by a pore size

distribution analyzer (Porolux™ 100, IBFT, Germany).

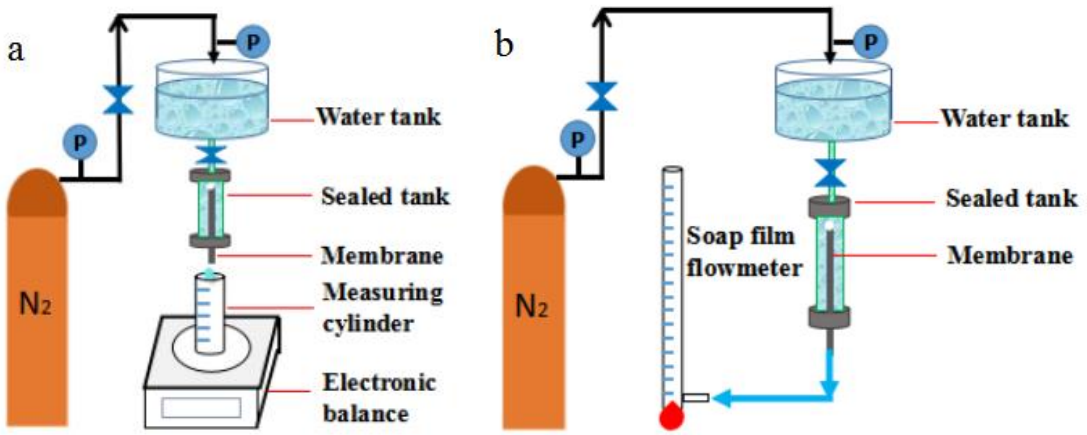

Figure S19. Schematic diagrams of the experimental apparati: (a) liquid entry pressure test and (b) N_2 permeability test.

To gain a better understanding of how the CNT distribution state influences the pore size and water/gas permeation properties, pore size distribution and water/gas permeability were studied and compared for PC-CNT and FC-CNT membranes (Fig. S20).

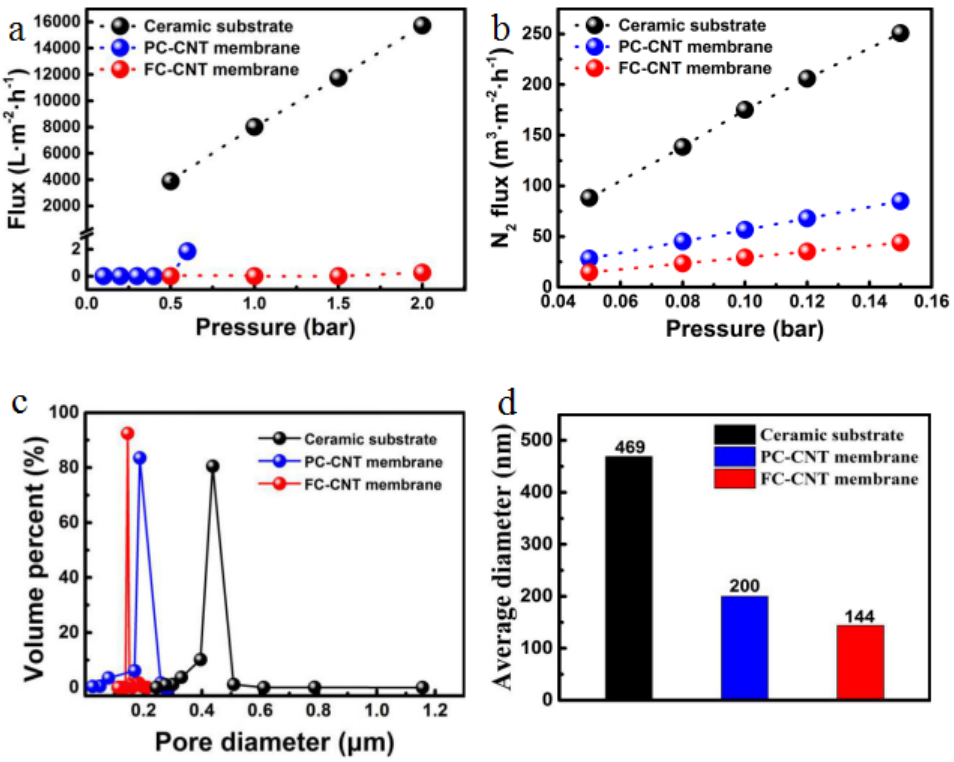

Figure S20. (a) Pure water permeability, (b) N_2 gas permeability, (c) pore size distribution and (d) average pore size for hollow fiber spinel-based ceramic substrate, PC-CNT and FC-CNT membranes.

S3 Performance of ceramic-CNT composite membranes

S3.1 Materials and chemicals

Sodium chloride (NaCl, analytical pure grade) and humic acid (HA, reagent pure grade) were obtained from Shanghai Aladdin Bio-chem Technology Co. Ltd. and Tianjin Guangfu Fine Chemical Research Institute, China respectively. Deionized water was produced in our laboratory using a double stroke ion exchanger (YF 02-01, Green Water Treatment Technology Co. Ltd., China).

S3.2 Electrochemical characterization of ceramic-CNT membranes

The electrochemical properties were evaluated using a 4-point conductivity probe (OAI Instruments, San Jose, CA) and cyclic voltammetry (CV) using a potentiostat (CH Instruments, Austin, TX). CV measurements were performed using a 3-electrode setup, with PC-CNT membrane as the working electrode, a platinum mesh as the counter electrode, and Ag/AgCl as a reference, 100 mM of $NaClO_4$ as the background electrolyte, at the scan rate of 50 $mV \cdot s^{-1}$. The 4-point conductivity measurement indicates that the *in situ* growth of CNTs on/inside the ceramic substrate results in enhanced electrical conductivity. The ceramic substrate behaves as an electrical insulator with a sheet resistance in excess of 10^{10} Ω/□.□ In contrast, the FC-CNT membrane exhibited a sheet resistance of 405.8±127.4 Ω/□. These results demonstrate that when the ceramic substrate is fully covered by CNTs, a percolating network structure is formed, allowing for electrical conductivity and subsequent electrochemical reactions for anti-fouling. Because the ceramic substrate did not exhibit any electrical conductivity, CV measurements were only performed on the FC-CNT membrane (Fig. S21). Limited electrolysis was observed when the potential reached -0.9 V (hydrogen evolution) and 1.6 V (oxygen evolution) vs. the Ag/AgCl reference. Thus, the FC-CNT membrane is able to facilitate electrostatic interactions in water once an external potential is applied, which makes it useful as an anti-fouling membrane under e-DCMD (Fig. 4).

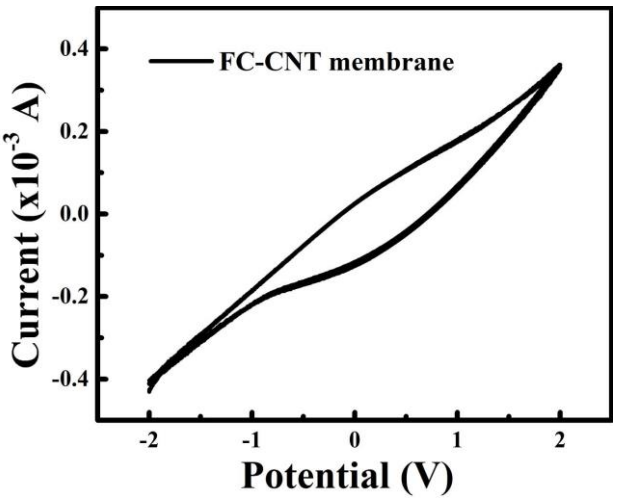

Figure S21. CV curves of FC-CNT membrane conducted in the presence of 100 mM $NaClO_4$ at a scan rate of 50 mV·s^{-1}.

S3.3 e-DCMD performance tests

The DCMD performances of ceramic-CNT composite membranes were assessed in a laboratory-made e-DCMD unit (Fig. S22) with and without electrochemical assistance. In an e-DCMD cell, a whole-cell potential of ±2 V was applied with the FC-CNT membrane serving as a cathode (anode) and a titanium mesh as counter electrode. In this study, the test membrane was placed into a module operating in a counter-current cross-flow mode. The MD experiments were conducted with simulated seawater (35 g·L^{-1} NaCl), high salinity water (70 g L^{-1} NaCl, 105 g L^{-1} NaCl, 70 g L^{-1} NaCl mixed with 30 mg L^{-1} humic acid (HA) as the feeds, and with deionized water (with a conductivity of around 0.01 μS·cm^{-1}) in the distillate tank. Three feed temperatures were evaluated (60, 70 and 80 °C), while the distillate was maintained at 20 °C. All the experiments were repeated in triplicate using three membranes and the relative standard deviation of these measurements was found to be less than 5%. The water vapor flux (J, L·m^{-2}·h^{-1}) of the membrane was calculated by

Eq. S3:

$$J = \frac{m}{A \cdot \rho \cdot t} \quad (S3)$$

Where m (kg) is the weight of distillate water at a given time t (h), A is the effective area of the membrane (m^2), and ρ is the water density (0.9982 $kg \cdot L^{-1}$, 20 °C).

The salt rejection (R) was determined according to *Eq. S4*:

$$R = \left(1 - \frac{C_p}{C_f}\right) \times 100\% \quad (S4)$$

Where C_f and C_p are the conductivities of the feed and distillate solutions, respectively, which were measured by using a conductivity meter (DDS-307A, INESA, Shanghai, PR. China)

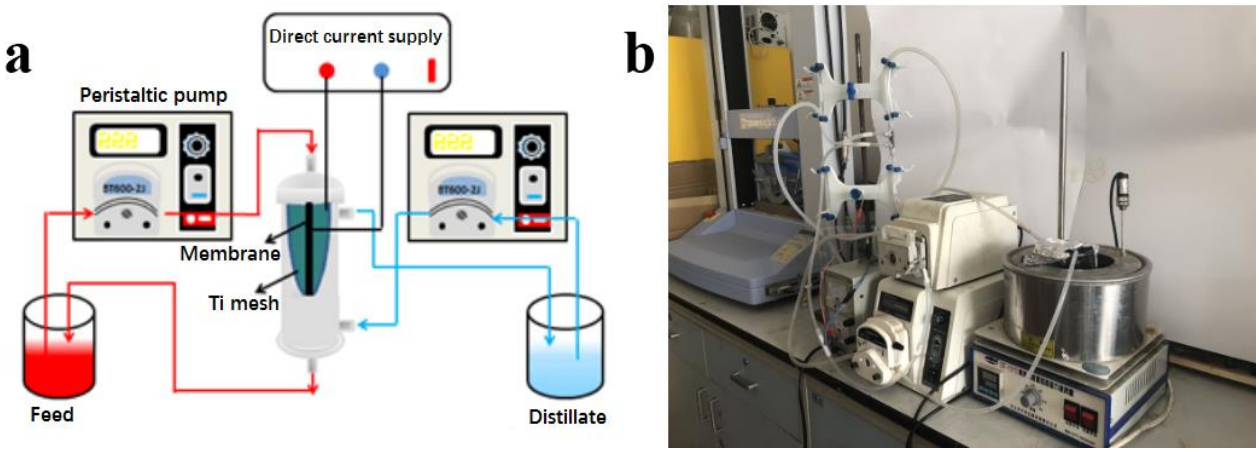

Figure S22. Schematic diagram (a) and a photograph (b) of e-DCMD apparatus for testing the ceramic-based CNT membranes fabricated in this work.

One common concern for the high thermal conductivity of CNT is that the energy efficiency (EE) may be low in DCMD. This reflects the heat efficiency and energy consumption of membrane distillation. The EE of a membrane is calculated by *Eq. S5*[15]:

$$\mathrm{EE}(\%) = \frac{J \cdot H_v \cdot A}{F \cdot C_p \cdot (T_{in} - T_{out})} \quad (S5)$$

Where J (kg·m^{-2}·h^{-1}), A (m^2) and F (kg·h^{-1}) are water flux, effective membrane area and mass flow rate, respectively. H_v (J·kg^{-1}) is the enthalpy of evaporation, and C_p (J·kg^{-1}·°C^{-1}) is the specific heat capacity of the feed solution. T_{in} and T_{out} (°C) are the temperatures of the feed and distillate, respectively.

S3.4 Membrane wetting for PC-CNT and FC-CNT membranes

The PC-CNT and FC-CNT membranes after 18 h DCMD operation (35 g·L^{-1} NaCl, ΔT = 60 °C) were tested by SEM-EDS to confirm membrane wetting by probing the presence of sodium or chloride ions. Membrane wetting was confirmed by SEM-EDS analysis for PC-CNT membrane, where both Na and Cl signals were detected (Fig. S23a). For the FC-CNT membranes, which exhibit thermally stable superhydrophobicity and thus good anti-wetting property, no Na or Cl signals were detected even after a prolonged DCMD operation time of 18 h (Fig. S23b)

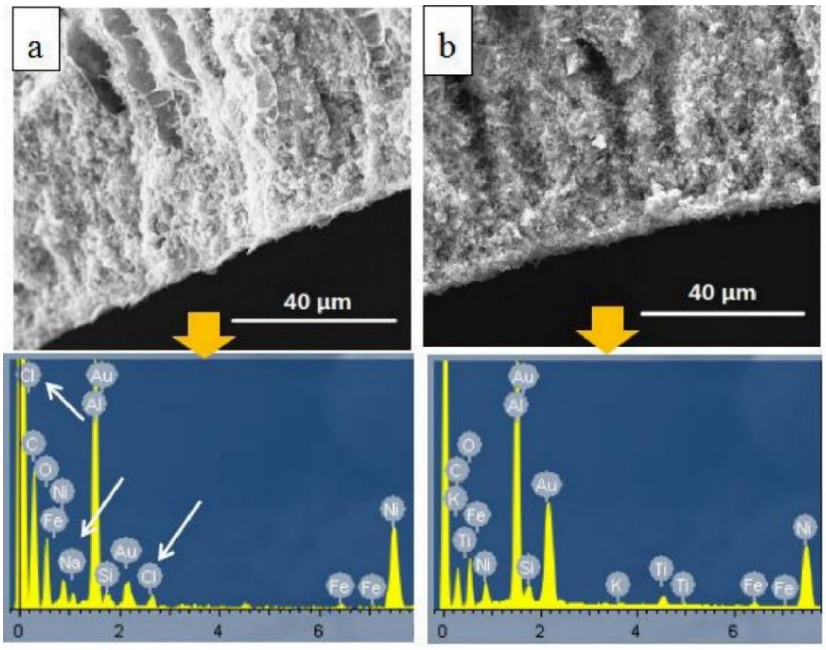

Figure S23. Cross-section SEM images and EDS spectra (scanned across whole cross-section of SEM images) of (a) PC-CNT and (b) FC-CNT membranes after DCMD operation (feed solution 35 $g \cdot L^{-1}$ NaCl, ΔT = 60 °C (feed temperature 85 °C and distillate temperature 25°C), operation time 18 h).

S3.5 Evaluation of energy efficiency and energy consumption

In spite of some expected thermal conductivity of CNTs, a superior energy efficiency of ~74.7% for the FC-CNT membranes in our study was obtained, indicating low heat loss, which is higher than hollow fiber CNT membranes (71.4%) and even higher than some polymeric membranes such as PVDF (67.7%) and PP (65.4%)[16]. This can be mainly ascribed to two reasons: (a) high water flux, much higher than existing inorganic MD membranes (Table S5) and (b) appropriate

membrane materials with specially designed morphological structure, which largely avoid heat loss during MD operation. In our work, a porous ceramic membrane substrate with very low thermal conductivity was employed for *in situ* construction of CNTs to form ceramic-CNT membranes. Most of the CNTs are located on the substrate surface and along the long channels of finger-like macro-voids (See Fig. 1, Fig. 2 and Fig. S23). Due to limited growth space, there are almost no CNTs grown in the sponge-like region, thus endowing low thermal conductivity over the whole ceramic-CNT membrane. In addition, the electrically conductive property of CNTs was exploited to improve MD desalination process efficiency performance, such as Joule self-heating, permeation flux and anti-fouling.

Even using direct current during e-DCMD, the energy consumption is low and is more than compensated with higher water productivity due to improved anti-fouling performance, which is calculated and demonstrated for our FC-CNT membranes under e-DCMC operation (shown as follows). In our work, a very low direct current potential (2 V) was employed on the FC-CNT membrane, which was used as the cathode. Although the use of direct current potential consumes energy, it is more than compensated by improvements in water flux due to its enhanced anti-fouling performance (Fig. 4c) and therefore it improves overall water production efficiency.

The concept “energy consumption per unit volume water production” is used for comparison of the FC-CNT membranes with and without applying electricity during the DCMD process using the following equation (*Eq. S6*).

$$W = \frac{(W_0 + W_e)}{J_1 / J_2} \quad (S6)$$

Where W (kW·h·m^{-3}) is the total energy consumed per unit volume water production with electric field, W_0 (kW·h·m^{-3}) is the energy consumed per unit volume water production without electric field (here W_0 =0.6 kW·h·m^{-3})[17], W_e (kW·h·m^{-3}) is the electrical energy consumed per unit volume water production with electric field, J_1 (L·m^{-2}·h^{-1}) is the water flux with electric field, and J_2 (L·m^{-2}·h^{-1}) is the water flux without electric field.

W_e can be calculated by the following equation (*Eq. S7*).

$$W_e = \frac{U \cdot (\frac{I}{A}) \times 10^{-3}}{J \times 10^{-3}} \cdot 1h \quad (S7)$$

Where W_e (kW·h·m^{-3}) is the electrical energy consumed per unit volume water production with electric field, U (V) is the direct current potential (2 V in our study), I (A) is the current measured, A (m^2) is the effective membrane area, J (L·m^{-2}·h^{-1}) is water flux.

In our study, W is calculated to be 0.5656 kW·h·m^{-3}, which is lower that W_0 (0.6 kW·h·m^{-3}), indicating that ~0.0344 kW·h·m^{-3} can be saved during e-DCMD using electric field. The result suggests that in order to produce the same volume water, the FC-CNT membrane under electrochemical assistance (direct current potential 2 V) can save ~5.74% energy consumption compared to that without electrochemical assistance. In addition, if no electricity is used, traditional backwashing cleaning with chemicals is more likely to degrade membrane structure and decrease performance.

S3.6 Performance comparison with other membranes

Some recently reported hydrophobic inorganic membranes for MD application[16, 18-28] are compared with the ceramic-CNT composite membrane in Table S5.

Obviously, the FC-CNT membrane outperforms in terms of both water contact angle (hydrophobic) and water flux while maintaining high salt rejection and highly thermal stability. Fluoroalkylsilane (FAS) is the most commonly used hydrophobic modifier for inorganic membranes (Al_2O_3, ZrO_2, Si_3N_4, and CNTs), which effectively enhances surface hydrophobicity, thus providing excellent salt rejection. However, besides imparting moderate water vapor flux and hydrophobicity, weak adhesion forces between FAS and inorganic membrane surfaces tend not to withstand long-term DCMD operation, resulting in the degradation of hydrophobic properties during prolonged or accelerated thermal stability tests (Fig. 3). With reference to the CNT-based bucky-paper class of membranes, [18, 19, 26] although the derived CNT network structures usually present abundant interconnected pores and high porosity, these membranes have very low permeation flux and moderate hydrophobicity levels. Alloy-mesh-CNT membranes exhibit high hydrophobicity (water contact angle = 163°) but low rejection (~90%).[24]

Interestingly, in the case of the FC-CNT membrane in our work, the flux exhibits a very high level of 37.1 $L \cdot m^{-2} \cdot h^{-1}$ for simulated seawater (35 $g \cdot L^{-1}$ NaCl, ΔT=60 °C), which is much higher than existing state-of-the–art inorganic DCMD membranes (Fig. 3 and Table S5). Even when the salt concentration was three times higher than sea water, the flux was still as high as 11.2 $L \cdot m^{-2} \cdot h^{-1}$ (even higher than other membranes when treating saline water of lower NaCl concentration, Table S5) with a rejection of 99.9% (Fig. 4a), indicating promising desalination performance for high salinity wastewater. Such high flux performance can be ascribed to the creation of a very large liquid-vapor interface (80.1±1.0% calculated surface porosity, > 9 times higher than unmodified membrane surface, Fig. S24) by surface CNTs layer which developed

during *in situ* growth of CNTs, as well as interior finger-like macrovoids. In combination, these two features accelerate the vaporization of hot feed solution and subsequent vapor transportation across the FC-CNT membrane during DCMD operation.

Table S5. Comparison of properties and MD performances for hydrophobic inorganic membranes between ceramic-CNT (FC-CNT) composite membrane fabricated in this work and those reported in the literature.

Membrane						Feed conditions		Performance		
MD	Material	Pore size (nm)	Contact angle (deg)	LEP (bar)	Configuration	[NaCl] ($g \cdot L^{1}$)	T ($^{\circ}C$)	Permeation flux ($L \cdot m^{-2} \cdot h^{-1}$)	Rejection (%)	Refs
DCMD	Spinel-CNT	144	170	2.0	hollow fiber	35	ΔT:60	37	>99.9	This work
DCMD	Bucky-paper	44	113.3	0.55	disc	35	ΔT:60	12	94.08	18
DCMD	Bucky-paper	-	140	4.41	disc	35	ΔT:70	9.5	>97	19
DCMD	Al_2O_3-FAS	290	141	5.61	disc	5.8	ΔT:53	2	>93	20
DCMD	ZrO_2-FAS	50	160	9	tubular	30	ΔT:90	4	99.8	21
DCMD	Al_2O_3-FAS	760	133	2	planar	20	ΔT:60	19.1	99.5	22
DCMD	Si_3N_4-FAS	740	136	3	hollow fiber	40	ΔT:60	10.5	>99	23
DCMD	CNT-FAS	199	168	4.5	hollow fiber	35	ΔT:80	30	99.98	16
DCMD	CNTs-alloy	-	163	-	mesh	10	ΔT:75	33	>90	24
DCMD	YSZ-FAS	100	135	2	planar	60	ΔT:40	9.2	>99	25
VMD	Bucky-paper	20.4	155	-	disc	35	ΔT:80	8	99.9	26

VMD	Al_2O_3-FAS	700	130	2	hollow fiber	40	ΔT:80	42.9	99.5	27
SGMD	Si_3N_4-SiNCO	-	142	-	disc	40	ΔT:75	6.5	>99	28

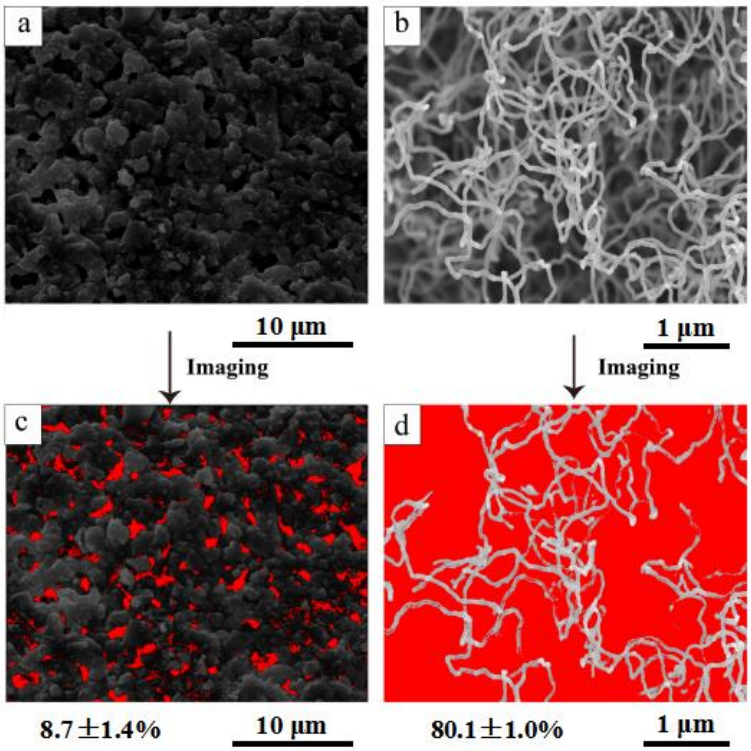

Figure S24. Surface SEM images of the hollow fiber spinel-based ceramic substrate (a) and FC-CNT membrane (b), and processed images of spinel-based substrate (c) and FC-CNT membrane (d) by Image J software. The red area in Figs. S24c and S24d denotes surface porosity.

To further demonstrate the superhydrophobicity (Figs. 2 and 3), Fig. S25 shows how a water droplet on a needle tip successively interacted with the surface of the FC-CNT membrane when the needle was brought close to and then drawn away from the membrane surface. The water droplet showed no tendency to spread on the membrane surface, but maintained its original shape even when pushed onto the

surface under compressive force by the needle.

Figure S25. Water contact angle test sequence for FC-CNT membrane surface.

Thermogravimetric analysis of FC-CNT membrane was performed in air between 30 and 800 °C with a constant heating rate of 10 °C·min^{-1}. The result in Fig. S26 indicates the FC-CNT membrane has good thermal stability up to 500 °C in air.

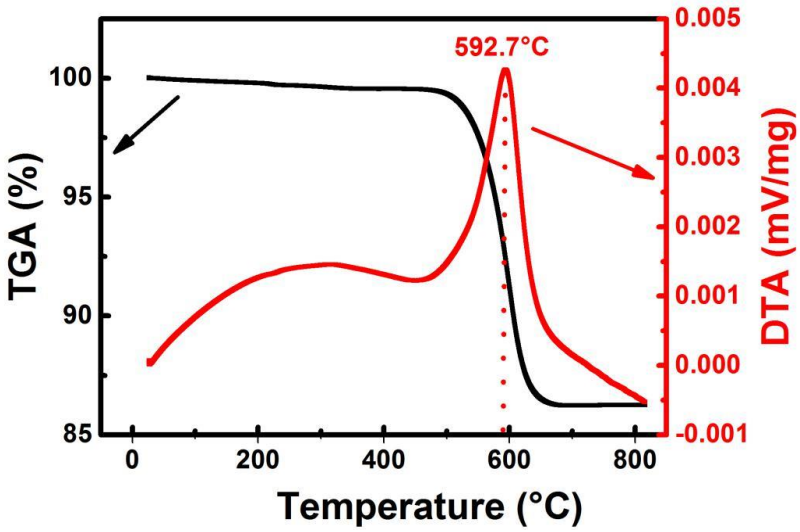

Figure S26. Thermogravimetric and differential thermal analysis of FC-CNT membrane (30-800 °C, constant heating rate 10 °C·min^{-1}, in air).

S3.7 Effect of feed temperature on performances for FC-CNT membranes

Water vapor flux and salt rejection (probed by ion conductivity) for FC-CNT membranes are represented in Fig. S27 as a function of feed inlet temperature. Due to an increase of trans-membrane vapor pressure difference, high inlet temperature

results in high flux. An excellent and consistent rejection of ~99.9% is observed (very low ion conductivity of < 0.1 μS·cm^{-1}) in the distillate at all the temperatures due to the excellent thermal stability and superhydrophobicity of the FC-CNT membrane.

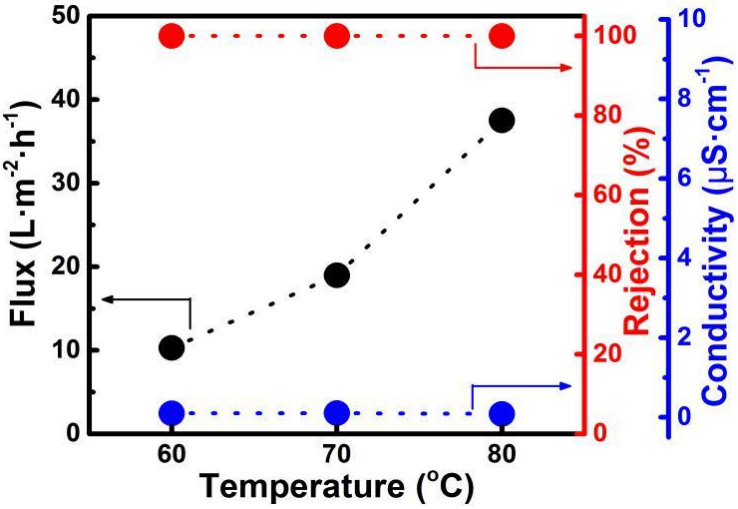

Figure S27. DCMD performances of water flux, salt rejection and distillate conductivity as a function of temperature difference between feed and distillate solutions ranging from 60 to 80 °C for FC-CNT membranes.

S3.8 Safety assessment of FC-CNT membranes for DCMD application

To assess any possible environmental risk of the developed FC-CNT membranes in water treatment due to the existence of some metal ions such as Al, Fe, Ni and Mn in the membrane starting materials (Table S1), the leaching behavior of Al, Fe, Ni and Mn ions was studied. The concentration of these metal ions in the distillate water after DCMD operation (35 g·L^{-1} NaCl, ΔT=60 °C, 18 h) was measured using ICP-MS (Inductively coupled plasma mass spectrometry, Nex ION 300D, PerkinElmer Inc., USA). The results shown in Table S6 clearly show very low levels of these metal ions, consistently meeting the standard of drinking water criterion issued by World Health Organization (Guidelines for drinking-water quality fourth edition, WHO, 2011),

assuring the safety of the DCMD and eDCMD processes in the present work. The very low levels of metal ions present in the distillate are attributed to the stabilization of major metal ions such as Ni and Al into the spinel crystalline lattice during the sintering process, along with stabilization of trace amounts of other metal ions such as Fe and Mn [2].

Table S6. Concentration of selected metal ions in the distillate solution after DCMD operation (35 $g \cdot L^{-1}$ NaCl, ΔT = 60 °C (feed temperature 85 °C and distillate temperature 25°C), operation time 18 h).

Concentration ($\mu g \cdot L^{-1}$)	Al	Fe	Ni	Mn
FC-CNT membrane	0.0042	0.0021	nd	nd
Drinking water criterion (WHO)	0.2	0.3	0.07	0.1

nd – not detected

S4. Preliminary extension to other inorganic membrane systems

The design strategy to achieve high performance thermally stable membrane structures is broadly applicable since the approach can be extended to other advanced ceramic membrane materials, due to the presence of –OH groups inherent on metal-oxide ceramic substrate surface, which provide active sites for loading nano-catalyst for *in situ* growth of CNTs. A more common robust ceramic membrane, α-alumina, has been also used as substrate for the fabrication of alumina-CNT membranes (Fig. S28), showing superhydrophobicity characteristics with CNT surface layers (~10 μm) fully covering the substrate.

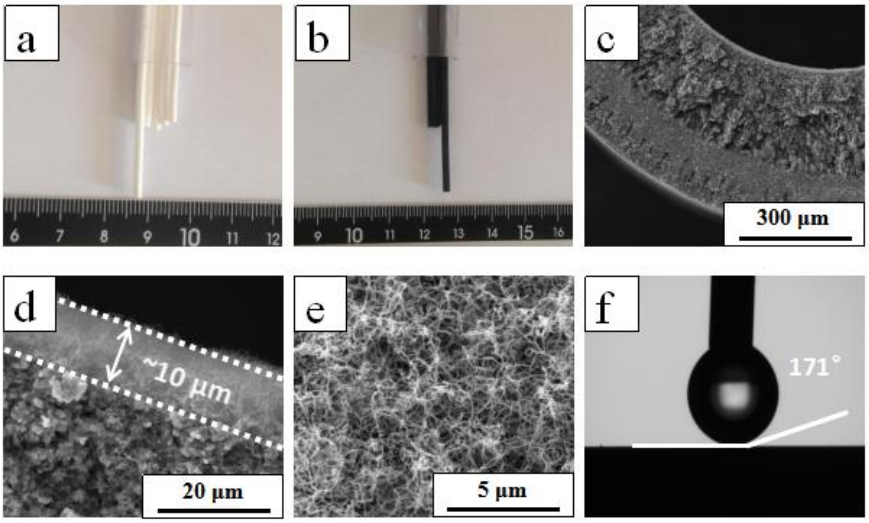

Figure S28. Photographs of the hollow fiber alumina ceramic substrate (a), alumina-CNT membrane (b), SEM images of fiber cross-section (c), enlarged fiber cross-section showing outer aspect with a CNT network layer of ~10 µm thickness (d), outer CNT network membrane surface (e) of alumina-CNT membrane and water contact angle result (f) of alumina-CNT membrane surface.

References

1. Chung, F. H. *J.Appl. Crystallogr.* **1974,** 7, 526-531.
2. Shih, K.; White, T.; Leckie, J. O. *Environ. Sci. Technol.* **2006,** 40, 5077-5083.
3. Vasanth, D.; Pugazhenthi, G.; Uppaluri, R. *J. Membr. Sci.* **2011,** 379, 154-163.
4. Zhu, L.; Chen, M.L.; Dong, Y.C.; Tang, C. Y.; Huang, A.S; Li, L.L. *Water Res.* **2016,** 90, 277-285.
5. Fung, Y.-L. E.; Wang, H. *J. Membr. Sci.* **2014,** 450, 418-424.
6. Kingsbury, B. F.; Li, K. *J. Membr. Sci.* **2009,** 328, 134-140.
7. Paiman, S. H.; Rahman, M. A.; Othman, M. H. D.; Ismail, A.; Jaafar, J.; Aziz, A. A. *Ceram. Int.* **2015,** 41, 12543-12553.
8. Ke, X. B.; Zhu, H. Y.; Gao, X. P.; Liu, J. W.; Zheng, Z. F. *Adv Mater.* **2007,** 19, 785-790.
9. Parham, H.; Bates, S.; Xia, Y.; Zhu, Y.Q. *Carbon.* **2013,** 54, 215-223.
10. Chen, X.W; Hong, L.; Xu, Y.F.; Ong, Z. W. *ACS Appl. Mater. Interfaces.* **2012,** 4,

1909-1918.

11. Ma, L.L.; Dong, X.F.; Chen, M.L.; Zhu, L.; Wang, C.X.; Yang, F.L.; Dong, Y.C. *Membranes* **2017,** 7, 16.
12. Venugopal, A.; Kumar, S. N.; Ashok, J.; Prasad, D. H.; Kumari, V. D.; Prasad, K.; Subrahmanyam, M. *Int. J. Hydrogen. Energy.* **2007,** 32, 1782-1788.
13. Chen, J.L; Li, Y.D.; Li, Z.Q.; Zhang, X.X. *Appl. Catal. A: Gen.* **2004,** 269, 179-186.
14. Piao, L.Y.; Li, Y.D.; Chen, J.L.; Chang, L.; Lin, J. Y. *Catal. Today.* **2002,** 74, 145-155.
15. Dudchenko, A. V.; Chen, C.; Cardenas, A.; Rolf, J.; Jassby, D. *Nat. Nanotechnol.* **2017**,12, 557-563.
16. Fan, X.F.; Liu, Y.M.; Quan, X.; Zhao, H.M.; Chen, S.; Yi, G.; Du, L. *J. Membr. Sci.* **2016,** 514, 501-509.
17. Vanneste, J.; Bush, J. A.; Hickenbottom, K. L.; Marks, C. A.; Jassby, D.; Turchi, C. S.; Cath, T. Y. *J. Membr. Sci.* **2018,** 548, 298-308.
18. Dumée, L. F.; Sears, K.; Schütz, J.; Finn, N.; Huynh, C.; Hawkins, S.; Duke, M.; Gray, S. *J. Membr. Sci.* **2010,** 351, 36-43.
19. Dumée, L.; Germain, V.; Sears, K.; Schütz, J.; Finn, N.; Duke, M.; Cerneaux, S.; Cornu, D.; Gray, S. *J. Membr. Sci.* **2011,** 376, 241-246.
20. Hendren, Z.; Brant, J.; Wiesner, M. *J. Membr. Sci.* **2009,** 331, 1-10.
21. Cerneaux, S.; Strużyńska, I.; Kujawski, W. M.; Persin, M.; Larbot, A. *J. Membr. Sci.* **2009,** 337, 55-60.
22. Ren, C.L.; Fang, H.; Gu, J.Q.; Winnubst, L.; Chen, C.S. *J. Eur. Ceram. Soc.* **2015,** 35, 723-730.
23. Zhang, J. W.; Fang, H.; Wang, J. W.; Hao, L. Y.; Xu, X.; Chen, C. S. *J. Membr. Sci.* **2014,** 450, 197-206.
24. Ashraf, A.; Salih, H.; Nam, S.; Dastgheib, S. A. *Carbon.* **2016,** 106, 243-251.
25. Liu, T.; Lei, L.B.; Gu, J.Q.; Wang, Y.; Winnubst, L.; Chen, C.S.; Ye, C.S.; Chen,

F.L. *J. Eur. Ceram. Soc.* **2017,** 37, 2431-2438.

26. Dumée, L.; Campbell, J. L.; Sears, K.; Schütz, J.; Finn, N.; Duke, M.; Gray, S. *Desalination.* **2011,** 283, 64-67.
27. Fang, H.; Gao, J.F.; Wang, H.T.; Chen, C.S. *J. Membr. Sci*. **2012,** 403, 41-46.
28. Wang, J. W.; Li, L.; Gu, J. Q.; Yang, M. Y.; Xu, X.; Chen, C. S.; Wang, H. T.; Agathopoulos, S. *AICHE J.* **2016,** 63, 1272-1277.